Surface finish classification using depth camera data

Automation in Construction 129 (2021) 103799

Contents lists available at ScienceDirect

Automation in Construction

journal homepage: www.elsevier.com/locate/autcon

Surface finish classification using depth camera data

Valens Frangez *, David Salido-Monzú, Andreas Wieser

Institute of Geodesy and Photogrammetry (IGP), ETH, Zürich, Switzerland

ARTICLE INFO

Keywords:
Surface classification
Surface roughness
Reflectance model
Depth camera
Automated inspection

ABSTRACT

We propose a novel approach for surface finish classification of digitally fabricated structures using an industrial depth camera. Data collected at different viewpoints are jointly processed to derive the spatial distribution of features describing the reflectance, which is in turn related to the surface finish. The features can be used to classify the surfaces according to their finish e.g., for assessing the homogeneity or conformance. We apply the method to four sprayed plaster specimens of similar visual appearance but different roughness. Using nearest neighbor classification we achieve an accuracy of 97% for the plaster samples. The approach is a contribution towards real-time quality inspection in digital fabrication.

1. Introduction

The last few years have seen a rapid growth of interest in robotically assisted construction,[1] where established construction processes are being automatized and digitized with the aim of replacing human labor with robotic tools in design, fabrication, assembly, and maintenance tasks [1]. One of the major challenges is to establish methods for automatically inspecting the quality of the fabricated structures [2–5].

Robotic spraying of concrete or plaster is a technique for digital fabrication that will largely reduce the need for expensive single-use formwork, increase productivity and enable mass production as well as production of bespoke elements. The quality of the produced structures does not only depend on the overall dimensional accuracy but also on fine details such as the surface finish and its homogeneity throughout the entire object [6,7]. Even though the desired finish may currently still be achieved by manual treatment of the surface using special tools, the surface inspection should be automated. Fig. 1 shows examples of a robotically sprayed surface (left), a robotic spraying setup (middle), and manual application of the concrete onto a curved wall (right). In general, surface finish is not only important because of the visual appeal of the structure and the resulting texture, but also because of the durability, adhesion, and interlocking of consecutive layers [8,9]. Surface roughness, a measurable quantity which indicates the level of surface finish, is well defined with existing standards such as DIN 4760 [10], which categorizes the surface shapes, or ISO 4278 [11], which establishes computation methods for profile roughness parameters (e.g. maximum profile peak height).

The most established method for surface finish assessment currently relies on manual and subjective analyses carried out by experts [12], using mechanical measurement tools such as stylus profilometers. An alternative approach to these is the sand patch test [13], where sand is applied to a circular surface patch. The average depth estimation and therefore roughness of the surface is calculated by division of the sand volume by the patch area. One of the major disadvantages of the technique, however, is its low repeatability, with a typical user-dependent variability of up to 20% [14]. A laser profilometry method which compares well to the sand patch test performance was presented in [14]. This approach provides higher repeatability but is still very tedious due to long manual measurements, cannot scale to large structural components, and provides only 2D information. Alternative solutions for replacing such tedious tasks with an areal, non-contact, non-destructive and most importantly automatic way are starting to get addressed in recent works for existing concrete structures [8,12] and particularly in 3D-concrete printing applications [2]. To the author's knowledge, however, no method with prospective potential to fully replace the manual procedures has been presented yet.

Surface classification based on reflectance properties has been extensively investigated in recent years within a wide range of applications, including construction, mostly driven by research in computer vision. Recent works, such as the one presented in [15], demonstrate surface-based material classification supported by extraction of reflectance parameters from terrestrial laser scanning (TLS) intensity data. They demonstrate that including reflectance estimations as an additional feature compared to only 3D and RGB information improves the

* Corresponding author.
E-mail address: valens.frangez@geod.baug.ethz.ch (V. Frangez).

[1] "Shaping the future of construction: a breakthrough in mindset and technology", World Economic Forum (WEF), Switzerland, 2016.

https://doi.org/10.1016/j.autcon.2021.103799
Received 23 December 2020; Received in revised form 2 March 2021; Accepted 7 June 2021

overall result of classification of construction materials. The relevance of retrieving reflectance information for segmentation, classification, and feature extraction applications was demonstrated as well in [16–18]. Furthermore, [19] presented a novel approach for classifying marls and limestones based on intensity data, and [20] showed that reflectance data can be efficiently used for moisture detection within building concrete walls. Innovative approaches for measuring concrete surface finish with regular RGB camera-based systems have been presented in [21,22]. [23] proposed image-based classification of surfaces for error detection using neural networks for robotic plastering. All these investigations demonstrate that the measured intensity contains information of the scene that is particularly related to the surface properties, and can be thus exploited for its classification. Active techniques as employed by time-of-flight (ToF) instruments (e.g. terrestrial laser scanners or depth cameras) largely mitigate the dependence on environmental illumination conditions. Additionally, such techniques allow capturing different information like geometric and radiometric one simultaneously and from a single location [15,24]. Since the surface finish of objects heavily influences the backscattered light recorded by the instrument [25], impacting both the points clouds [26] and the intensity data, it can as well be used for its evaluation.

In this paper we propose a new method for automatic quality assessment of surfaces on millimetre-level roughness features, based on multi-view data acquired with an industrial depth camera. Particularly, we (i) establish a method to retrieve surface reflectance values based on a model compensating for the influences of distance, angle of incidence (AOI), and inter-pixel variations, using the acquired point clouds and intensity images of the scene; (ii) introduce a method to estimate the normalized reflectance, directivity and spatial variability of the reflectance; and (iii) apply the proposed methods to distinguish between sprayed plaster specimens with different surface roughness as a case study targeting applications in digital fabrication. The proposed approach uses a combination of the intensity and geometric information from a multi-view acquisition setup to derive more informative reflectance-related features than in other presented approaches, thus establishing a promising basis for more accurate and comprehensive surface analysis. Our approach offers a solution for non-destructive, non-contact, optical-image based portable measurements. It is not limited to flat walls but can be used to evaluate surface finish of more complex geometries, such as for example free-form surfaces and geometries with sharp edges or boundaries.

The proposed method is described in detail in Section 2. The instrument specific calibration process developed specifically for the depth camera used in this study is given in Section 3. The sensitivity analysis of the estimated features is evaluated in Section 4. The results, presented and discussed in Section 5, validate the proposed approach and show one of its possible applications. Finally, the main conclusions and outlook of this work are given in Section 6.

2. Methodology

The proposed method combines the geometric and radiometric information contained in depth camera observations of the surface under test from different viewpoints to derive spatially-distributed surface features related to its reflectance and scattering properties. Fig. 2 summarizes the proposed processing pipeline from data acquisition to surface description.[2]

The input data consist of depth camera acquisitions of the same surface from a minimum of two viewpoints. Each acquisition consists of a point cloud representing the surface geometry, and intensity images containing information on the surface reflectance. For each viewpoint, the point cloud is used to estimate the relative orientation of the surface with respect to the camera as an AOI estimation per pixel. The intensity image, after calibration of the instrumental systematic influences is concurrently used to estimate the absolute reflectance underlying each pixel.

Afterwards, the estimated values corresponding to the same surface patch observed from different viewpoints, associated via co-registration, are used as an input to a scattering model. This results in two features per pixel: the surface normal absolute reflectance R_0, indicating the maximum value of the absolute reflectance pattern of the underlying surface, and the scattering coefficient n, modelling its diffuseness. The variability of the estimated reflectances is used in parallel to derive a third feature providing additional information on the surface inhomogeneity. Such surface description based on its reflectance properties can be used for robust classification of different surface finishes and, potentially, for regression of a standardized metric of surface roughness.

2.1. Data acquisition

2.1.1. Depth camera technology

The term depth camera applies to instruments implementing one of various technologies used to acquire 2D depth images of the observed scene [30]. With additional knowledge about the camera optical system, these 2D images can be transformed into 3D point clouds, offering a practical and fast method to acquire the geometry of the environment with mm- to cm-accuracy over distances up to several meters.

Most of the commercially-available time-of-flight (ToF) depth cameras rely on observations of the accumulated delay on an intensity modulated signal emitted from the camera to illuminate the complete scene and measured independently on each camera pixel. After calibration of instrumental systematic errors, these delays can be used to estimate the average distance from the camera to the patch of surface covered by each pixel. In addition to the depth information, the

Fig. 1. A concrete spraying robotic setup [7] (left); a robotically applied plaster layer [6] (middle); achieving desired finish by manual treatment of a sprayed surface, NCCR Digital Fabrication, 2018 (right).

[2] The implementation of the method and all the processing was done in Python using the libraries Numpy [27], Scipy [28], and Scikit [29].

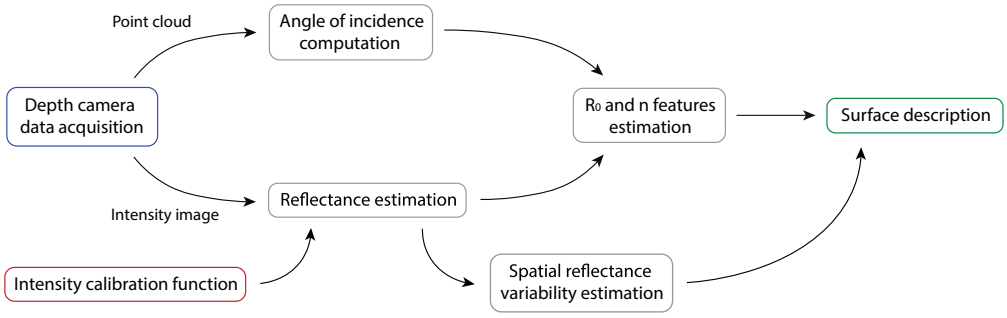

Fig. 2. Processing pipeline for the surface description based on estimated surface reflectance and scattering features derived from multi-view depth camera data.

amplitude of the reflected signals is also typically computed and provided as an intensity image. Both observations are derived from a signal actively illuminating the environment, thus being largely independent on the external illumination conditions when compared to passive systems such as regular RGB cameras. This provides a significant advantage over these regular cameras regarding measurement robustness for the type of application envisioned in this work, where challenging environments with changing illumination conditions such as construction sites or fabrications workshops are targeted. The practical limitations of the achievable accuracy mainly arise from variability of the operating conditions (mostly environment temperature) and multipath effects depending on the scene geometry [31]. Performance assessment procedures of commercially available depth cameras primarily addressing these limitations can be found in [32]. Many of these error sources can be largely reduced by calibration or mitigated through a careful design of the acquisition geometry when allowed by the application.

The data collection in this investigation was carried out using a state-of-the-art industrial ToF depth camera Helios Lucid [33]. The most relevant specifications for the presented analysis of this camera are listed in Table 1. A performance evaluation and a data quality assessment for this camera are presented in [3]. Significant errors may be obtained when the camera is used within its warm-up time. We therefore allocated sufficient warm-up time before each measurement session for all the data acquired for the present investigation. Furthermore, we demonstrated in [3] that the edges of the point clouds acquired using this particular depth camera are affected by significantly larger deviations. To avoid contamination of the results by these deviations, we only use the central part (320 × 480 pixels) of the images (480 × 640 pixels) herein.

2.1.2. *Multi-view acquisition and transformation*

The data acquisition consists of depth camera observations from different viewpoints. While a minimum of two viewpoints are needed, additional viewpoints contribute to reduce the uncertainty of the computed features. This uncertainty is also reduced when the different viewpoints provide observations of the surface with significantly different AOIs, e.g. quasi-normal observations together with tilted ones. We analyze this experimentally in Section 4.

The acquisition at different viewpoints can be carried out simultaneously if more than one depth camera is available, or sequentially as long as the investigated surfaces and surface properties are sufficiently time-invariant. This is, if no significant change of the relevant surface properties occurs while hardening within the time span between different acquisitions. While this is hard to quantify without specific knowledge of the applied material, surface geometry is generally stable after a few seconds from fabrication and relevant changes in reflectance occur on minutes-to-hours scales. Aside from reducing complexity and cost, the sequential acquisition is a particularly attractive solution for digital fabrication if a camera can be mounted on the robot arm to acquire data during the fabrication process exploiting the robot movement to reach multiple viewpoints.

Once acquired, the information from the different views has to be co-registered, i.e. aligned with respect to the reference view, to establish correspondences between observations of the same area in the scene. To achieve this, all the intensity and AOI images (see Section 2.2.1) are transformed. Herein, we arbitrarily use the respective first image. This transformation is carried out by image warping [34], i.e. an image transformation method based on detection of identical points within pairs of images. The warping of the images introduces the additional need for interpolating the values of pixels of the transformed image that fall in-between different values of the original one. In this work a bi-linear interpolation was selected experimentally as an adequate solution to implement this step. It is worth noting that the co-registration process can be simplified in applications where the relative positions of the cameras are known. This is for instance the case in robotic fabrication, where the transformations between views can be carried out based on the recorded robot poses. Herein a simplified registration process was used assuming planar surfaces, future work will either introduce processing in 3D instead of 2D or deal with the co-registration by projecting the points from one point cloud onto the image plane of the other camera using the collinearity equations.

Fig. 3 shows an example of the transformation for two viewpoints. The bright quadrilateral areas near the center of images (a and b) correspond to the same area viewed from two different viewpoints. Image 3b is transformed into 3c taking image 3a as a reference. Once all available images have been transformed in this way, the information underlying corresponding pixels in different images belong to the same surface area and can thus be analyzed jointly for the feature

Table 1
Selected specifications of Helios Lucid ToF depth camera [33].

Precision	0.5 mm (<0.5 m); 2.2 mm (<1.5 m)
Accuracy	± 5 mm for up to 1.5 m
Resolution	640 × 480 pixels
Field of View (FoV)	59° x 45°
FoV Area [m^2]	0.27 at 0.4 m; 1.66 at 1.0 m
Illumination	850 nm (IR laser diodes)
Range	Up to 6 m
Point Density [points/dm^2]	~2900 at 0.4 m; ~460 at 1.0 m

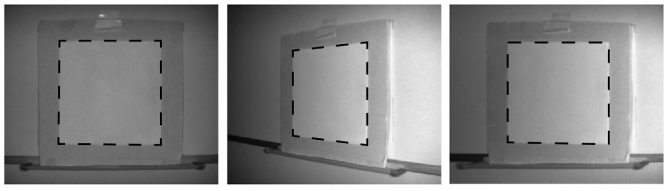

Fig. 3. Example of two intensity images of the same area acquired using a Helios Lucid ToF depth camera at different viewpoints (a and b). The central image b is transformed taking the left one as a reference by warping, producing the right image c.

computation.

2.2. Data transformations

2.2.1. Angle of incidence

The AOI θ_i corresponding to the individual pixel i is the angle between the surface normal $\vec{n}_i$ and the viewing direction $\vec{v}_i$ associated with that pixel (see Fig. 4), which can be expressed as

$$\hat{\theta}_i = arccos\left(\vec{v}_i \cdot \vec{n}_i\right) \tag{1}$$

The vector $\vec{v}_i$ is uniquely defined by the pixel position and the camera geometry. It points from the camera's origin to the point P_i of the point cloud. The normal vector $\vec{n}_i$ is calculated from a local plane approximation to all points within a neighborhood of P_i, in correspondence with established standard algorithms (see e.g., [35]). The accuracy of $\vec{n}_i$ depends on the point cloud accuracy and a trade-off between the selected size of the neighborhood P_i and the complexity of the underlying geometry. Using large areas for the local plane approximation is desirable to increase averaging of the noise on the individual points, hence reducing its impact. If the selected neighborhood, however, is too large in relation to the underlying surface geometry, the fitted plane may not represent the local surface properly.

The output of the AOI estimation process is one image per viewpoint, in which each pixel contains the corresponding estimate $\hat{\theta}_i$. As an example, Fig. 5c and d shows the AOI images corresponding to the two depth images shown in Fig. 3a and b.

2.2.2. Absolute reflectance

The transformed intensity images are used to derive the reflectance for each pixel, i.e. the proportional amount of reflected light from a measured surface relative to the used instrument's scale, which can be expressed for a certain AOI or more commonly for normal incidence [36]. The reflectance is then used to estimate the absolute reflectance, which is expressed with respect to a calibrated diffuse reflectance standard such as a Spectralon target, and is thus a quantity that can be compared irrespective of the instrument used for its acquisition [36]. Other approaches to estimate reflectance are shape from shading [37], photometric stereo [38], and albedo estimation [39]. Deriving absolute reflectance from intensity is possible because the measured intensity at each pixel is proportional to the amplitude of the illumination signal received by the pixel after having been backscattered by the surface. It is therefore influenced by the surface reflectance at the corresponding viewing angle, the intensity distribution of the illumination signal, the distance, and the detection efficiency of the camera. The measured intensity I_i and the absolute surface reflectance $R(\theta_i)$ at the AOI θ_i for a pixel i are related as follows:

$$R(\theta_i) = \frac{I_i}{f_i(d_i, \theta_i) \cdot k}, \tag{2}$$

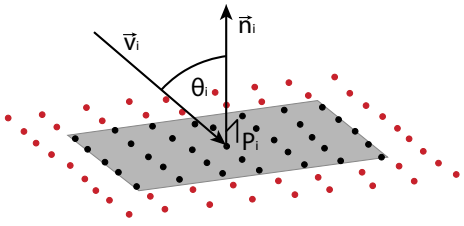

Fig. 4. Diagram of the AOI computation for a random point i within a point cloud using the camera viewing angle vector $\vec{v}_i$ and the surface normal $\vec{n}_i$ estimated by patch-wise plane fitting and the resulting θ_i. The plane fit was done to a point neighborhood marked in black, while remaining surrounding points are marked in red.

where k denotes a radiometric scale factor, and $f_i(d_i, \theta_i)$ models the impact of emitted power (illumination), distance, pixel-dependent attenuation, and detection efficiency depending on angle of incidence. The output of the absolute reflectance estimation process is one image per viewpoint, in which each pixel contains the estimated absolute reflectance of the corresponding surface for the AOI at which it was observed. Two examples of raw intensity images of the same planar target taken from different viewpoints are shown in Figs. 6a and b. The corresponding absolute reflectances are shown in Figs. 6c and d.

2.3. Feature estimation

2.3.1. Surface Normal reflectance and scattering coefficient

We have defined our model following a simplified version of established approaches that divide surface reflectance in a diffuse component and a specular one of varying directivity (see e.g. [40]). Our model consists on two parameters, namely the surface reflectance R_0 for normal incidence and the scattering coefficient n:

$$R(\theta) = R_0 \cdot cos\left(\left[2 - \frac{1}{n}\right] \cdot \theta\right)^n. \tag{3}$$

These two jointly estimated features represent the reflection properties of the area underlying the respective pixel. The defined model represents a reduced-complexity hybrid between a perfectly Lambertian scatterer ($n = 1$) and a perfectly specular reflector ($n \to \infty$). Increasing values of $n > 1$ thus represent increasingly specular and decreasingly diffuse reflection. The simplicity of the model was preferred over more complex representations to enable estimations of the parameters with limited number of observations. An example of a more complex model is given in [40], which includes additional parameters to model both the Lambertian and specular reflectance properties independently and more accurately. The absolute reflectances and AOI values calculated from the range and intensity images (see Sections 2.2.2 and 2.2.1), along with the correspondence of pixels in different images established through the image transformation (Section 2.1.2), are now used to estimate R_0 and n for each surface element via least-squares adjustment.

The results of this adjustment can be collected in feature images (one for R_0 and one for n), i.e. an image showing spatially mapped features which were computed for each pixel. We filter these images spatially using a Gaussian filter to reduce the impact of observation noise, while still retaining the spatial distribution of the features.

Fig. 7 represents the measurement process for different surface reflectances and viewing angles. In Fig. 7 (left), a certain pixel of the camera (in this case represented by the camera axis) observes the surface with an AOI θ, thus acquiring a signal proportional to the reflectance $R(\theta)$. The dashed part of the lines represents the component of the reflectance pattern measured from that viewpoint. A similar example is given in Fig. 7 (right) for a more specular surface reflecting most of the incoming light in a narrow pattern in the direction opposite to the incidence one according to Snell's law. The maxima of the reflected pattern for the two illustrated viewing angles are indicated with dotted lines, whereas the observed reflectances $R(\theta)$ are again depicted with dashed lines. Further increasing the AOI θ_2 of the second view in this case would result in very low returned signal. In both cases, adding more viewpoints to observe the same surface area would yield a more complete sampling of the reflectance pattern of the surface, which can in turn be exploited to model the surface reflectance properties more accurately.

2.3.2. Spatial reflectance variability

A third feature, namely the spatial reflectance variability, is included in our approach to capture the inhomogeneity of the reflectance in the vicinity of each pixel and its neighborhood by analyzing how reflectance varies over the surface specimens. It represents a joint indicator of the the variability of the normal reflectance and diffuseness of the surface.

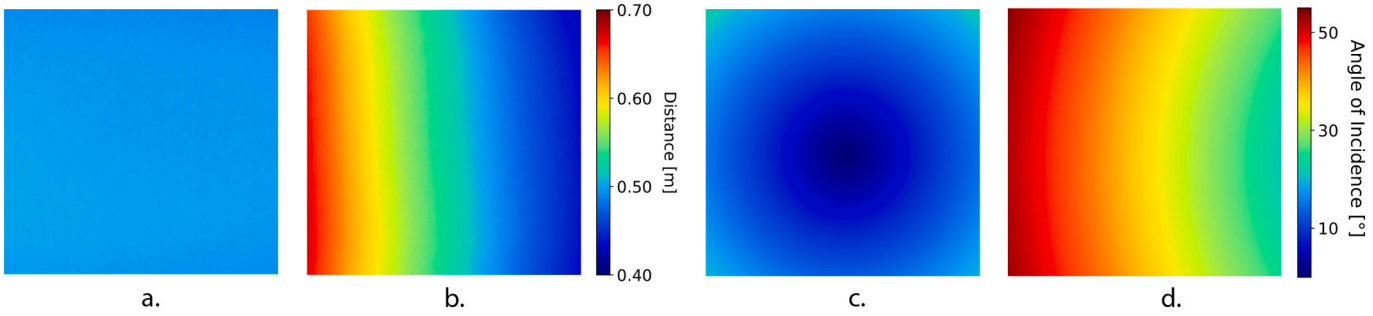

Fig. 5. Two examples of AOI estimation images from two viewpoints on a planar target (c and d) and their corresponding depth images (a and b).

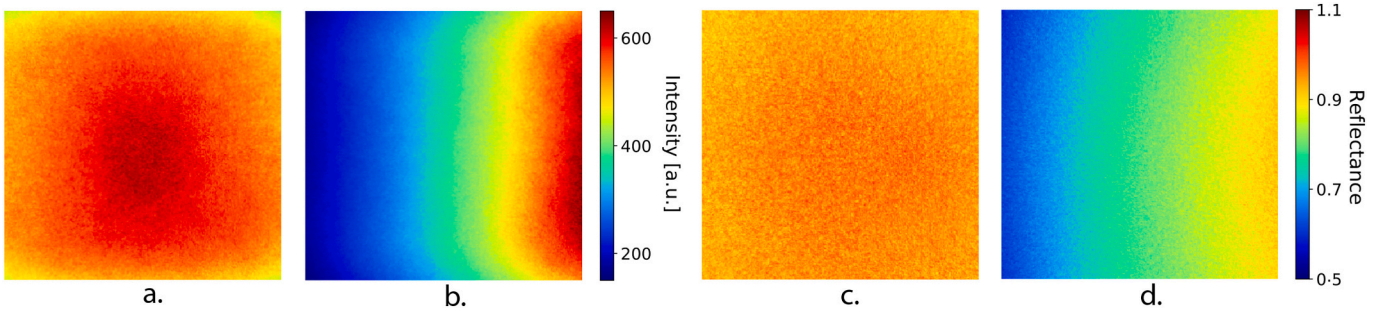

Fig. 6. Two examples of raw intensity images (a and b) of a planar target taken at different viewpoints like in Fig. 3, and the resulting AOI-dependent absolute reflectances (c and d).

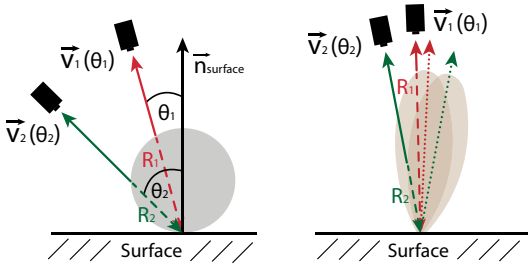

Fig. 7. Lambertian reflectance (left) and mostly specular reflectance (right) examples. Both showing surface observation at two different θ, sampling the reflectance pattern resulting in R (dashed line).

This feature is estimated by convoluting the most perpendicularly acquired reflectance image with respect to the scene (i.e. with the camera axis at quasi-normal incidence on the surface), which was corrected for the effect of the Lambert cosine law. The convolution is done with a filter computing standard deviation of the input values, which depends on the defined filter kernel size.

Higher reflectance variability values and therefore corresponding image areas are assumed to be associated with stronger roughness changes compared to the rest of the surface due to the interaction of the illumination signal with the irregularities within the surface finish [25]. As explained in Section 2, the intensity recorded by each pixel is an integral over the illumination signal on the pixel area, meaning variation in surface finish affects the measured intensity values.

3. Empirical calibration model

The objective of the intensity calibration is to recover absolute reflectances of the scanned surface by eliminating the impact of the AOI and distance due to the measurement configuration, and the instrument related inter-pixel variations, thus isolating the effect of the reflecting surface. Based on this, a function $f\left(\widehat{d}_i, \widehat{\theta}_i\right)$ is defined, which is considered different for each pixel but constant over time for the used specific camera. The parameters of f_i can be determined experimentally before applying the camera for surface assessment. The input to the estimation of the intensity function fit are AOI, intensity, and Z-coordinate values.

A calibration dataset was acquired on a flat and homogeneous diffuse white wall to model the aforementioned parameters. The flatness of the calibration surface was validated with a plane fit to a point cloud acquired with a high-end TLS (Leica P50), producing an empirical standard deviation of orthogonal deviations of below 1 mm over the whole area of approximately 2 m × 2 m, considered sufficient for the presented study. The surface material was selected to closely emulate an ideal Lambertian scatterer, which was validated by direct comparison on the intensity images using a calibrated diffuse reflectance standard (Spectralon 60%). The assumed reflectance pattern of that surface enables separation of the impact of viewing angle caused by the camera from that introduced by the surface itself. Point cloud and intensity data were acquired using the depth camera at different viewpoints and orientations. The distances range from about 0.3 m to 1.0 m and the AOI varies

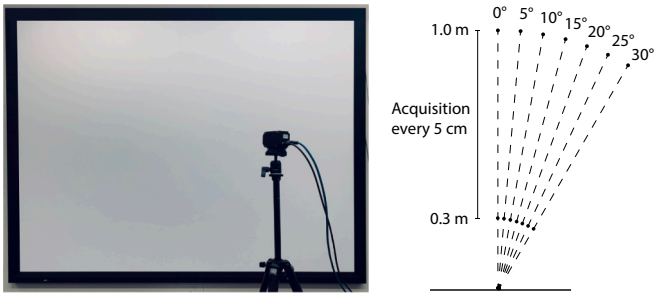

Fig. 8. Configuration for the acquisition of the calibration dataset covering approximately distances from from 0.3 m to 1.0 m and camera pointing angles (viewing direction of central pixel) from 0° to 30°.

within a range of 30° per pixel (see Fig. 8).

The acquired intensity data are first corrected for the known Lambertian reflection of the calibration surface:

$$I_i^{\text{corr}} = \frac{I_i}{cos(\theta_i)}. \tag{4}$$

The information in all the corrected intensity images is then merged and mapped as a function of distance and AOI, both estimated from the point cloud data following the same procedure for the AOI as described in Section 2.2.1. The mapped corrected intensities $I_i^{\text{corr}}(d_i, \theta_i)$ represent the calibration data per pixel underlying the instrumental function $f_i(d_i, \theta_i)$ to be modelled.

A physically induced model considering a reduction of detected power inversely proportional to the distance squared was chosen to model the impact of distance d_i. Following an empirical evaluation of different possibilities, a second degree polynomial yielded better results in modelling the impact of the AOI θ_i with respect to higher degree polynomials and was therefore selected. The general calibration model $f_i(d_i, \theta_i)$ is then defined as

$$f_i\left(\widehat{d}_i, \widehat{\theta}_i\right) = \left(A_i + \frac{B_i}{\widehat{d}_i^2}\right) \cdot \left(C_i \cdot \widehat{\theta}_i^2 + D_i \cdot \widehat{\theta}_i + E_i\right), \tag{5}$$

where A_i, B_i, C_i, D_i, and E_i are the model coefficients to be estimated by fitting on the mapped corrected intensity data $I_i^{\text{corr}}(d_i, \theta_i)$. As an example, the fitted function is shown for a randomly chosen pixel in Fig. 9.

The average coefficient of determination for all pixels was 0.98 indicating that the model fits the data well. Correlation between the parameters was computed and is given in Table 2. Most of the parameters show very low correlation, which indicates a high separability between them. This is not the case for parameters C and D, which are highly negatively correlated. This suggests potential for reducing the model complexity, thus slightly improving computational efficiency if required by the targeted application.

The significance of each of the estimated parameters within the function fit in eq. (4) was computed by introducing the same level of variability to each of the parameters. The results indicate that the most significant parameters in the model, i.e. their change influencing the estimation the most, are B and D. Furthermore, the variability in % of each of the parameters over the whole image was computed, being 8.94, 3.92, 1.79, 1.38, and 4.44 for A, B, C, D, and E, respectively. The computed values support the decision for estimating the intensity function fit per pixel and not using a single function for the whole image, which would not represent the calibration data accurately.

Finally, the computed intensities were referenced to the calibrated reflectance standard, with known absolute reflectance of 60% for the operation wavelength of our camera. This allows for computing the scale factor k which converts the intensity measurements of the camera into absolute reflectance values:

$$k = \frac{R_0(\text{Spectralon})}{0.6}, \tag{6}$$

where R_0(Spectralon) is the ratio between measured intensities on the Spectralon and the surface used for acquiring the calibration dataset under the same conditions. The estimated absolute reflectance $\widehat{R}_i\left(\widehat{\theta}_i\right)$ can then be calculated for each pixel i using eq. (2).

To further verify the calibration and gain additional insights into its performance, the calibration function was evaluated on one of the images of the calibration dataset by comparison with the corresponding corrected intensity image obtained according to eq. (4), the latter representing a ground truth of the expected result if all instrumental effects are ideally compensated. The reflectance estimate is shown in Fig. 10 (left), where maximum deviations of about 8% are visible. The spatial correlation of the deviations indicates that approximately 3% are associated to residual systematics. This shows that, while most of the instrumental effects are effectively compensated for with the proposed calibration, there is some room for improvement if required by the application. A more demanding application case than the one used herein may require increasing the calibration effort with extended data to fit a more complex calibration function.

The reflectance estimates of the previously used calibration dataset by using the implemented calibration function were then used to estimate the n and R_0 features. The input data to that estimation, absolute reflectance $\widehat{R}_i$ and AOI $\widehat{\theta}_i$, are shown on a polar plot in Fig. 10 (right), together with the reflectance of an ideal Lambertian scatterer for reference (red). The agreement between the estimated values and the assumed reflectance pattern of the calibration surface shows the successful calibration. The normal reflectance R_0 and scattering n features were calculated as described in Section 2.3.1. The empirical standard deviations of R_0 and n are approximately 0.005 and 0.008, respectively. Furthermore, the achieved function fit result and its application to the case study (see results in Section 5) performed very well in terms of providing input of sufficient quality for feature estimation, which resulted in homogeneous estimates for the same type of surfaces.

Table 2
Correlations between the parameters used in the intensity function fit (see eq. (4)).

	A	B	C	D	E
A	1.0	0.14	0.16	−0.12	−0.16
B		1.0	0.17	−0.14	−0.46
C			1.0	−0.99	0.09
D				1.0	−0.13
E					1.0

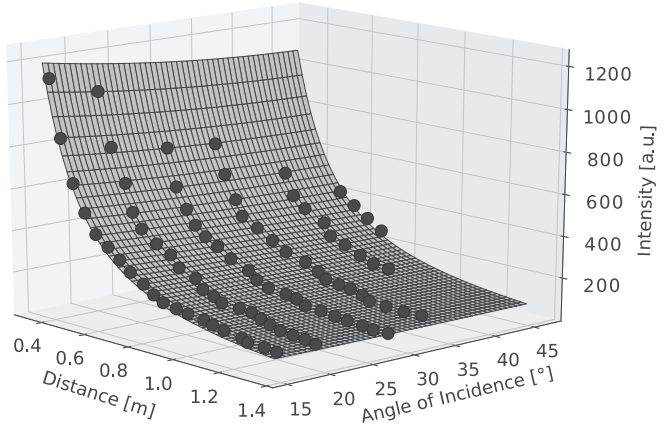

Fig. 9. An example fit of the calibration model per pixel $f_i\left(\widehat{d}_i, \widehat{\theta}_i\right)$ to the calibration intensity data $I_i^{\text{corr}}(d_i, \theta_i)$) for a random pixel i.

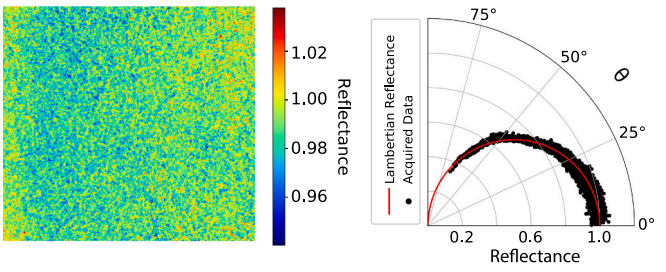

Fig. 10. Estimated reflectance values using a calibration function showing remaining variability within the image (a) on the dataset used for intensity calibration function. Polar plot (b) showing the input data which is used for estimation of the features. A red curve stands for a perfect diffuse reflectance, as was it was associated with the surface that was used in this analysis.

A second calibration dataset was acquired for the same target surface with a slightly different configuration of the measurements, i.e. a few cm and a few ° of differences in camera positions and orientations, respectively. The goal was to analyze the repeatability of the A, B, C, D, and E parameter estimates, and therefore of the overall calibration. The difference between them was computed as smaller than 1%, indicating a very good agreement between the parameters. Both sets of calibration parameters were used to estimate reflectances on a subset of the first calibration dataset and the variability between the reflectance estimates was on the level of 2.9%. Furthermore, these estimated reflectances were then used for estimation of the two features, i.e. R_0 and n. The variability between the estimates is on the level of 0.5% and 1.4% for R_0 and n, respectively. These small variations within the calibration parameters, reflectance estimates, and most importantly feature estimates show that the instrumental and configuration effects covered by the calibration are effectively time-invariant, and that our calibration approach can extract and model them repeatably.

4. Sensitivity analysis

A sensitivity analysis was carried out to quantify the influence of the noise in the input parameters $\widehat{R}_i$ and $\widehat{\theta}_i$ on n and R_0 depending on the measurement configuration. A Monte Carlo (MC) simulation was used for generating noisy input parameters for the model using two different noise levels of both intensity and AOI. The chosen simulation sample size was $M_{\mathrm{MC}} = 500$. Fixed values $n = 1$ and $R_0 = 1$ were selected as ground truth for the simulation, representing approximately typical values obtained on a preliminary assessment on the plaster samples used in the results. The absolute reflectance noise levels used were the minimum (min.) and maximum (max.) empirical standard deviations $\sigma_{\widehat{R}}$ of the estimated reflectance obtained during calibration, representing in turn the expected range of noise levels affecting the reflectance estimates in normal working conditions. For the AOI noise, those values were estimated as empirical standard deviations $\sigma_{\widehat{\theta}}$ of the AOI values obtained from the point cloud of a plane acquired from a distance of 0.4 m using the entire point cloud of the planar surface (for minimum standard deviation) and using only a small neighborhood (1 dm^2). The choice of the latter is relevant when non-flat surfaces are evaluated and the patches need to be sufficiently small, depending on the surface complexity. Both pairs of noise values are provided in Table 3. The remainder of this section summarizes the impact of the angular separation between the views and of the number of views on the deviations of the estimated features R_0 and n, computed as the mean and standard deviation of the errors derived from the MC simulation.

4.1. Impact of separation between views

For studying the impact of different angular separation between the camera views, we processed 10 different configurations of two views. In all the simulated cases, one camera angle was fixed at 45° while the second one was chosen in steps of 1° from 44° to 0°, producing M_{MC} simulated data sets with correct AOI but noisy reflectance for each of these configurations, and another M_{MC} data sets with correct reflectance but noisy AOI. Fixing one of the views at 45° aims at providing approximately worst-case scenario results within a range of practically useful viewing angles considering that: (i) the quality of the acquired data at larger viewing angles is expectably too low due to the low reflected signal for high AOI, and (ii) the sensitivity of both features—specially that of R_0 as can be concluded from inspection of the partial derivatives of the model—is very low for small AOIs, hence fixing a view close to normal incidence would yield a variability generally underestimated compared to an arbitrary combination of viewing angles.

Table 3
Minimum (min.) and maximum (max.) standard deviations used within MC simulation.

	Min. value	Max. value
$\sigma_{\widehat{\theta}}$ [°]	0.27	1.70
$\sigma_{\widehat{R}}$	0.015	0.040

The variability of both R_0 (Fig. 11a) and n (Fig. 11b) versus viewing angle separation for correct AOI indicates that the uncertainty of both depends strongly on the viewing angle separation, reaching errors over several tens of % on both parameters for viewing angles differing by less than 10°. Such errors make the estimated features not useful for any practical classification application, all plots in Fig. 11 are thus limited to 50% for better visibility of the areas with relevant values. Angle differences by about 20° or more are required in order to estimate both coefficients with an accuracy better than 10% if the reflectance noise level is high.

The variability of R_0 (Fig. 11c) and n (Fig. 11d) for correct reflectance but noisy AOI shows a similar trend with slightly smaller impact, i.e. errors in both coefficients below 10% are expected only for viewing angle separations smaller than 10°. In this case the results also show that the variability of both R_0 and n is better for angle differences close to 0° than for slightly larger ones. This is likely caused by a low model sensitivity to small angle differences. This point, however, has not been investigated further given that it holds no practical implications since very small angle differences are nevertheless unacceptable due to the variability introduced by reflectance noise.

Based on the outcomes of this first indicative sensitivity analysis, we conclude that measurement configurations should aim at getting significantly different views of the same area but avoid very large incidence angles where signal degradation is expected to increase noise too much in the input parameters, i.e. above 45°.

4.2. Impact of number of views

It is to be expected that additional views improve the quality of the estimates. Therefore we now extend from the 2 views of the previous subsection to $K > 2$ views. For simplicity, we assume that the viewing angles of the first and K^{th} camera span an angle of exactly 45° and the other views are equally spaced in between.

The influence of the noise in absolute reflectance versus the number of views on n and R_0 is shown in Fig. 12 (a and b). The results indicate that there are no relevant biases and the standard deviation of the estimated R_0 and n reduces approximately proportionally to $1\sqrt{N}$ and $1/N$ respectively when using N-times as many viewpoints.

The impact of noise in AOI depending on the number of views, shown in Fig. 12 (c and d) follows a similar behaviour. The precision of both R_0 and n improves with the number of viewpoints, being approximately proportional to $1/N$-times the increase of the number of viewpoints. Since one of the views $K = 2$ corresponds to 0°, the impact of the low sensitivity of R_0 to AOI when AOI is very small is visible in Fig. 12c for $K = 2$. This has again with no practical implication due to the much larger noise propagation of the intensity noise in such configuration.

Although only a small number of scenarios were investigated and a complete assessment of the expected sensitivity for any combination of viewpoints is not provided, the selection of the cases and noise values analyzed herein corresponds to a realistic practical setting, and thus serves as an approximated but useful indicator of the expected errors and trends for different configurations.

Following the sensitivity analysis results, five views were selected in the data acquisition in the following result section as a trade-off between feature accuracy and practical measurement complexity.

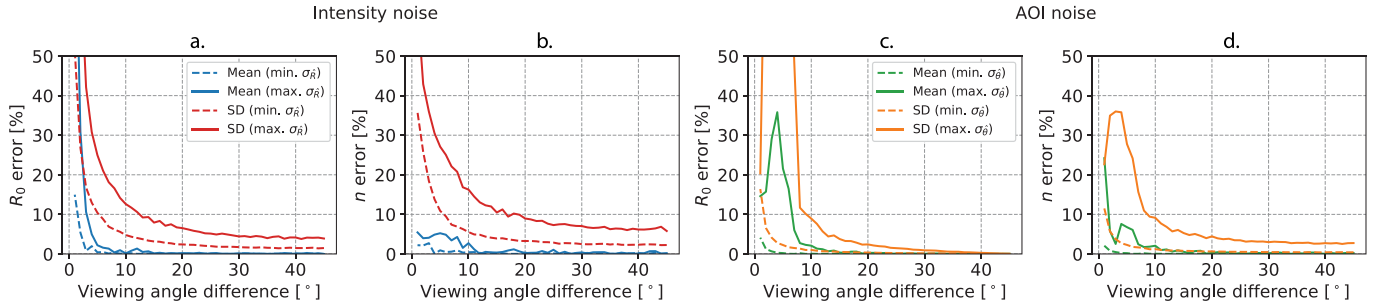

Fig. 11. Feature variability due to intensity and AOI noise as a function of angular separation between two viewing angles. Variability of normalized reflectance feature (a and c); variability of scattering coefficient feature (b and d). SD denotes standard deviation.

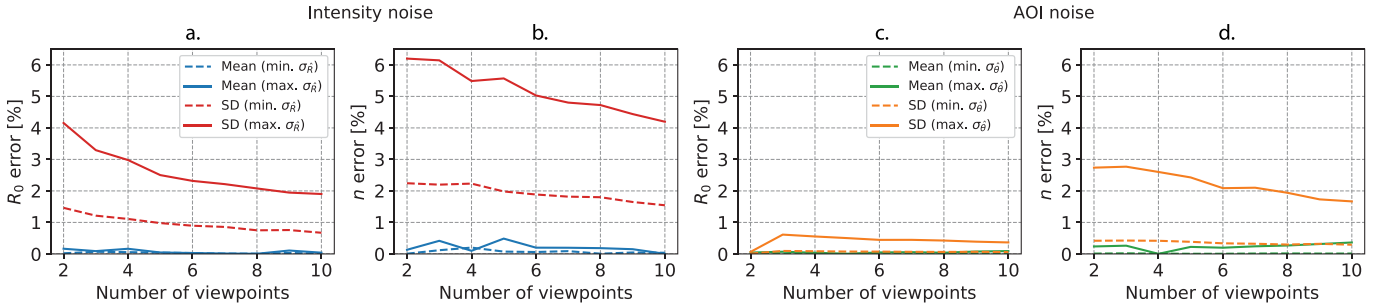

Fig. 12. Feature variability due to noise in the intensity and AOI as a function of number of viewpoints. Variability of normalized reflectance feature (a and c); variability of scattering feature (b and d). SD denotes standard deviation.

5. Results

5.1. Specimens and data acquisition

The proposed method was applied to demonstrate its potential for distinguishing between surface samples of the same material but with different surface finish, in particular different roughness. We used the four specimens of gypsum plaster, i.e., a building material extensively used for surface finishing of walls and ceilings, shown in Fig. 14 (left). The different surface roughness of the specimens is a result of different granularity of the sand used for the mix and of different spraying techniques. The specimens used in this section were not handpicked, however we assume the classification accuracy presented later on would decrease if we had more classes between S1 and S4, in particular more classes between S1 and S3.

Prior to the acquisition with the depth camera, each of the specimens was scanned using a GOM ATOS Core structured light scanner that, according to its calibration certificate, can provide point clouds with a spatial resolution of about 3500 points per cm^2 and an accuracy of approximately 10 μm per coordinate. The goal of these reference measurements was to quantify the respective surface roughness beforehand. A plane was fit to each of the resulting point clouds, and orthogonal deviations of the points with respect to a best-fit plane were computed for small patches of approximately 4 cm^2. This was done, as opposed to calculating the empirical standard deviation for a plane fit to the respective entire point cloud of the sample to account for non-planarity of the specimens. These orthogonal deviations were then used to compute the empirical standard deviations (ESD) given in Table 4. If the non-planarity would not be accounted for, it would bias the orthogonal distance computation and therefore increase the standard deviation estimate, leading to wrong results. A similar test by fitting a plane to the point clouds acquired with the depth camera was done as well, to check whether different surface roughness would affect the noise level of the point clouds. As shown in Table 4, no noticeable differences can be observed, achieving similar noise levels within the noise range specified for the device for all the specimens point clouds. Bigger patches of approximately 30 cm^2 were selected from the dataset acquired from the first view for this evaluation. The spatial resolution of the point cloud is about 150 points per cm^2.

Each of the specimens was scanned separately with the depth camera from five viewpoints with approximately the same setup configuration. In all these cases, the camera was oriented such that the single specimen was at the centre of the image. This assured similar measurement conditions across different acquisitions. All five views were co-registered as explained in Section 2.1.2. The absolute reflectances and AOIs were then estimated based on the input data as shown in Fig. 13 following the procedure described in Sections 2.2.2, 2.2.1, and 2.3.2. The results and their use for surface classification are presented and discussed below.

Table 4
Empirical standard deviations (ESD) of orthogonal distances from local best fit planes for each of the four specimens, using the structured light scanner and the depth camera.

Specimen	S1	S2	S3	S4
ESD (scanner) [mm]	0.0068	0.0255	0.0532	0.1459
ESD (depth camera) [mm]	0.91	0.88	0.87	0.94

5.2. Estimated features

The estimated features are displayed as an image in Fig. 13 (bottom, right) for one of the specimens. The samples were prepared manually, trying to achieve a homogeneous surface finish within each sample. The estimated values corroborate this with a span of only about 4% for n and 10% of R_0. The visible systematic pattern is very likely due to the residual deviations of the intensity calibration function fit and is not related to the actual surface finish inhomogeneities. An improved calibration function would reduce the systematics, however the following results indicate that it is already sufficiently good for the given application example.

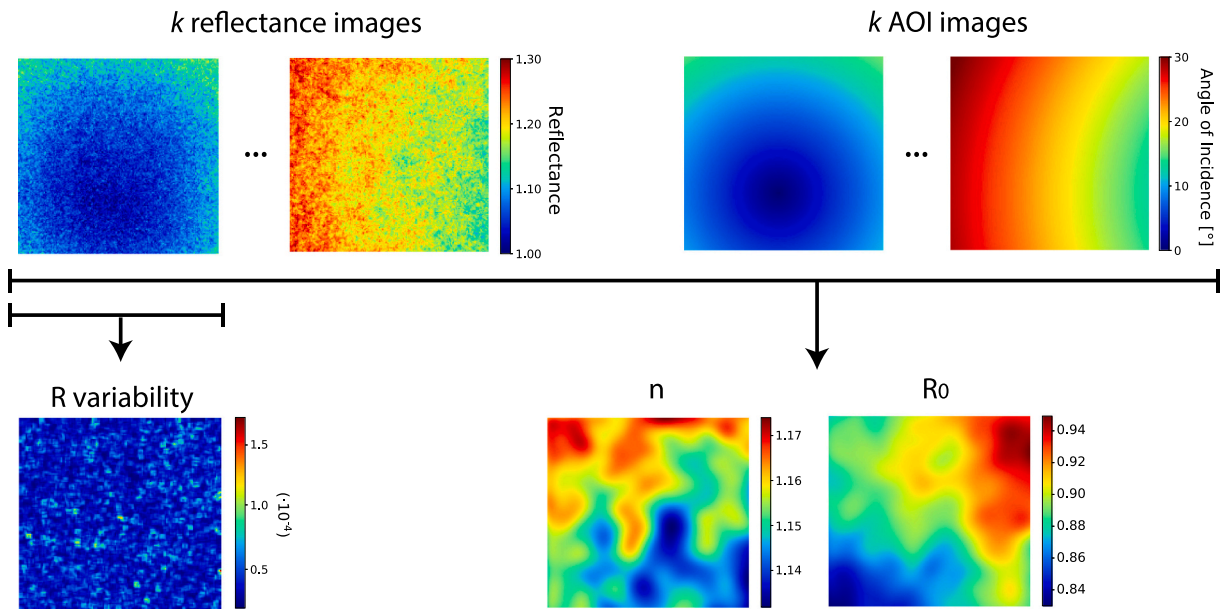

Fig. 13. The number of viewpoints use for data acquisition, i.e. m reflectance and AOI images (herein, $m = 5$), for estimation of the n and R_0 features. The reflectance variability feature is estimated using only the reflectance image from the first viewpoint.

Fig. 14 (middle) displays the computed features for all specimens in the 2D feature space of R_0 and n; different colors indicate the features of different specimens (see labels in Fig. 14, left). The figure shows that these specimens are clearly distinguishable in the feature space. Apparently, both features are useful for the distinction: while the value of n decreases with increasing surface roughness (from S1 to S4)—indicating in agreement with the expectation that the reflection gets more diffuse with increasing roughness—R_0 improves the separability of the specimens by assuring that the scatter plots associated with the individual specimens do not overlap in the feature space. The feature estimates shown on the figure are a result of smoothing with a Gaussian filter of size 7×7. This size roughly corresponds to a size of $5 \times 5\ \text{mm}^2$ at the surface of the specimens. This kernel size worked well for the given specimens and geometric configuration. Its optimization for less homogeneous surfaces requires addressing the trade-off between averaging noise-induced feature variability by using larger kernels while still capturing actual spatial variations of the surface features. More variable surfaces would generally require smaller kernels hence allow for less noise averaging at the feature level. The generalization of this optimization is proposed for future work.

Interestingly, there is a nearly linear relation between the average value of n per specimen and the surface standard deviations quantifying the respective roughness (see Table 4), but the normal reflectance does not show a similarly straightforward relation to the roughness. R_0 increases with increasing surface roughness for specimens S1 to S3 but then drops with increasing roughness and is similarly low for the roughest specimen S4 as for smoothest one.

Additionally, the spatial reflectance variability for each of the specimens was computed as explained in Section 2.3.2. The kernel used for this was the same size as for the estimation of the R_0 and n features, i.e. 7×7. All three features are visualized in Fig. 14. As apparent in the figure, the additional spatial variability feature enhances slightly the information on roughness, contributing to the separability of the surface specimens.

The 3D specimen features and their associated specimen labels were used in a machine learning approach based on a k-nearest neighbors (kNN) classifier. This then allowed for applying the learned features to another dataset to be able to classify them. All four specimens used in the training step were positioned within the scene (see Fig. 15) and a new dataset of data pairs was acquired at five random views, at different AOIs from ~0° to ~40° and distances approximately 50 cm away. This configuration differs from the one used for acquiring the reference dataset in viewpoints, which are approximately 15 cm farther from the samples, and in angles, which are different for about ~5° per viewpoint. The samples were as well rotated by either ~90° or ~180° with respect to their position in the reference configuration. The decision of using

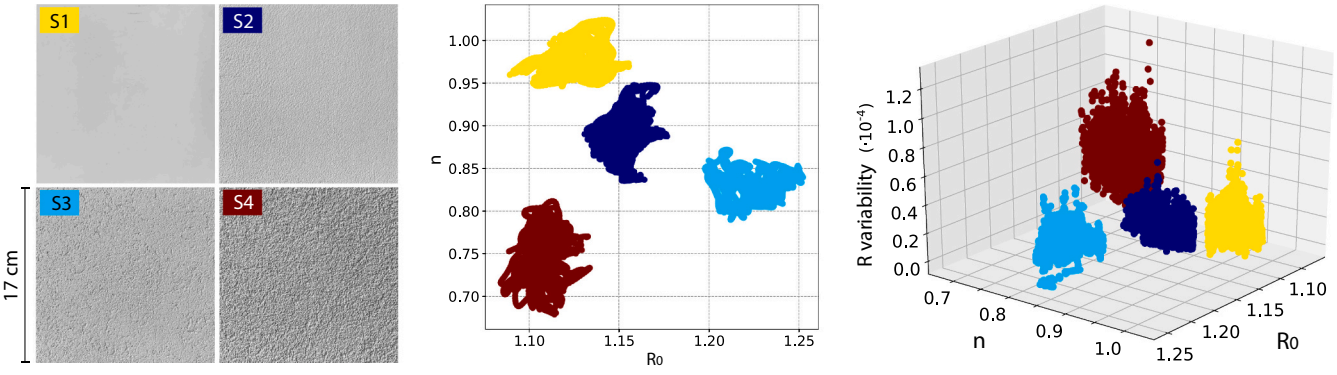

Fig. 14. Four specimens examples used in the study to demonstrate the applicability of the presented method (left). Estimated R_0 and n features (middle) also displayed together with surface reflectance variability for the four specimens(right).

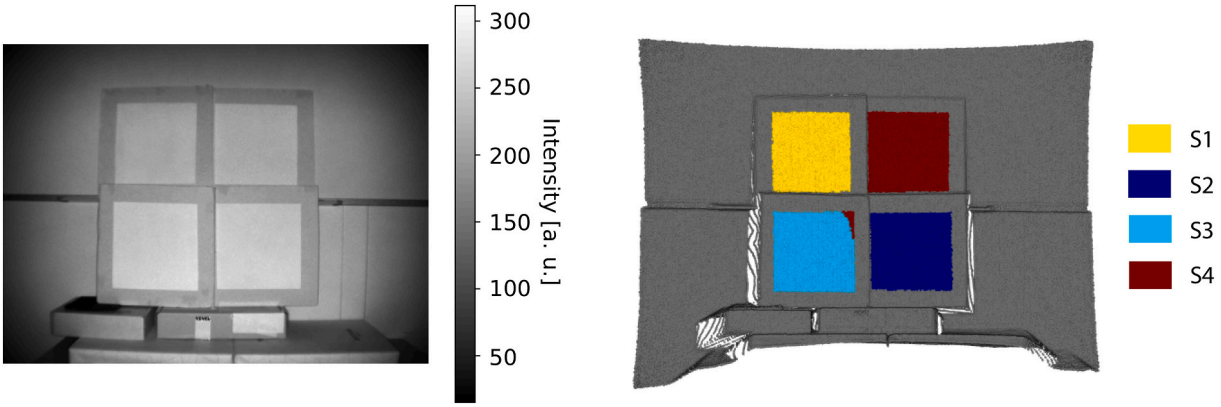

Fig. 15. Raw intensity image of the acquired scene with all four specimens included (left) and the corresponding point cloud with points colored according to the specimen label (right).

five views follows the results of the sensitivity analysis (see Section 4), selected as a reasonable trade-off between increasing estimation precision while still keeping the acquisition effort low. The features computed with five views exhibited a variability of approximately 10%, being slightly larger compared to the specimen reference dataset. A NN = 1 classification was applied to the estimated feature images to predict the labels on the specimens. The prediction step yielded approximately 97% of correct labels. These are mapped in the intensity image and shown in Fig. 15. These results indicate that the features were estimated with sufficient accuracy despite the different measurement geometry with respect to the training data, indicating the generalization potential of the approach to classify previously trained surface samples. Finally, the labeled images were filtered using a median filter and thus eliminating a few wrongly classified pixels resulting in fully correctly classification result.

The computational cost of data processing was evaluated for completeness. Processing five images for the results presented in this section required approximately 5 min using a Python script and a computer with 15.8 GB RAM and Intel Core i5-8279U CPU with 2.4 GHz. Every additional image increased the processing time by about 30 s. It is important to stress that no particular code optimization (by e.g. choosing a more suitable classifier with adequate inference performance) was done so far and that the implementation was not focused on the efficient implementation. Code optimization and implementation on dedicated hardware (e.g. FPGAs) for quasi-real-time operation will be addressed in future work.

6. Conclusion

We have developed and demonstrated a method to quantify surface finish based on reflectance and scattering properties estimated from multi-view depth-camera images. Calibrating the camera radiometrically before use, we succeed in decoupling pixel and distance dependent effects on the measured intensities from surface and angle-of-incidence dependent ones. Along with a transformation of several images, taken at different locations, into a common coordinate system, this allows estimating the normal surface reflectance, a scattering parameter and the reflectance variability on the object surface. These values can be used to assess the homogeneity of the surface finish of an object or to assess the correspondence of the actual to an intended finish.

An anticipated application case is roughness estimation for quality control of robotically fabricated plaster or concrete surfaces. We have experimentally applied the developed method to distinguish four plaster specimens with different surface roughness. We found a nearly linear relation between the surface roughness—at a scale below the geometric resolution of the depth-camera—and the scattering coefficient estimated from the depth-camera's data. Interestingly, a similarly simple relation between the normal reflectance and the surface roughness was not found; the smoothest and the roughest surface reflected less strongly than the surface specimens with medium roughness. However, jointly the estimated features showed clear separability of the specimens within the feature space. A nearest neighbor classifier was trained on these data and used on an additional dataset demonstrating a classification accuracy of 97%.

Although the proposed model can operate with only two views of the same surface area, we show that using more viewpoints largely increases the feature estimation accuracy. Considering the targeted application on robotic fabrication, where the camera can be mounted on the robot arm and move along with it, acquiring multiple views of each surface area does not require a significant additional effort. Additionally, the maximum size of the object that can be measured does not depend on the camera FoV but only on the working range of the robot arm.

The proposed approach can be used for automatic surface inspection in robotic fabrication in a non-contact and non-destructive way, making it ideal for evaluating large freshly produced surfaces, either off- or on-site. The performance of commercially available industrial-grade depth cameras is largely independent of environmental lighting conditions and they are thus suitable for the application proposed herein. Future work will focus on adapting the approach for handling more complex surface geometries. To this end, the approach of image warping shall be extended to a more sophisticated registration of acquired datasets, e.g. by using robot pose information for registering the respective depth camera datasets. Furthermore, the local surface model for AOI estimation shall be extended from the current plane approach to more versatile models such as 2D triangulation or smooth parametric functions. The demonstration of the proposal in an actual robotic fabrication process is also planned as future work.

Declaration of Competing Interest

None.

Acknowledgments

This research was supported by the NCCR Digital Fabrication, funded by the Swiss National Science Foundation (SNSF): NCCR Digital Fabrication Agreement #51NF40-182887. The authors would like to thank Selen Ercan Jenny (Gramazio Kohler Research, ETH Zürich) for providing the plaster surface finish specimens.

References

[1] T. Wangler, E. Lloret, L. Reiter, N. Hack, F. Gramazio, M. Kohler, M. Bernhard, B. Dillenburger, J. Buchli, N. Roussel, et al., Digital concrete: opportunities and

challenges, in: RILEM Technical Letters vol. 1, 2016, pp. 67–75, https://doi.org/10.21809/rilemtechlett.2016.16.
[2] R. Buswell, P. Kinnell, J. Xu, N. Hack, H. Kloft, M. Maboudi, M. Gerke, P. Massin, G. Grasser, R. Wolfs, et al., Inspection methods for 3d concrete printing, in: RILEM International Conference on Concrete and Digital Fabrication, Springer, 2020, pp. 790–803, https://doi.org/10.1007/978-3-030-49916-7_78.
[3] V. Frangez, D. Salido-Monzú, A. Wieser, Depth-camera-based in-line evaluation of surface geometry and material classification for robotic spraying, in: *37th International Symposium on Automation and Robotics in Construction (ISARC 2020) (virtual)*, International Association for Automation and Robotics in Construction, 2020, pp. 693–702, https://doi.org/10.3929/ethz-b-000446406.
[4] M. Kim, Noncontact Quality Assessment of Precast Concrete Elements using 3d Laser Scanning and Building Information Modeling, Ph.D. dissertation, 2017, https://doi.org/10.14711/thesis-b1450719.
[5] S. Neudecker, C. Bruns, R. Gerbers, J. Heyn, F. Dietrich, K. Dröder, A. Raatz, H. Kloft, A new robotic spray technology for generative manufacturing of complex concrete structures without formwork, Procedia CIRP 43 (2016) 333–338, https://doi.org/10.1016/j.procir.2016.02.107.
[6] S. Ercan Jenny, E. Lloret-Fritschi, F. Gramazio, M. Kohler, Crafting plaster through continuous mobile robotic fabrication on-site, Construct. Robot. (2020) 1–11, https://doi.org/10.1007/s41693-020-00043-8.
[7] N. Taha, A.N. Walzer, J. Ruangjun, T. Bürgin, K. Dörfler, E. Lloret-Fritschi, F. Gramazio, M. Kohler, Robotic aerocrete-a novel robotic spraying and surface treatment technology for the production of slender reinforced concrete elements, in: Architecture in the Age of the 4th Industrial Revolution-Proceedings of the 37th eCAADe and 23rd SIGraDi Conference vol. 3, eCAADeSIGraDi, 2019, pp. 245–254, https://doi.org/10.3929/ethz-b-000387276.
[8] L. Tonietto, L. Gonzaga, M.R. Veronez, C. de Souza Kazmierczak, D.C.M. Arnold, C. A. da Costa, New method for evaluating surface roughness parameters acquired by laser scanning, Sci. Rep. 9 (1) (2019) 1–16, https://doi.org/10.1038/s41598-019-51545-7.
[9] K. Gadri, A. Guettala, Evaluation of bond strength between sand concrete as new repair material and ordinary concrete substrate (the surface roughness effect), Constr. Build. Mater. 157 (2017) 1133–1144, https://doi.org/10.1016/j.conbuildmat.2017.09.183.
[10] DIN 4760:1982--06, Form deviations - concepts and classification system, Berlin, DE, Standard, 1982, https://doi.org/10.31030/1110827.
[11] DIN EN ISO 4287:2010--07, Geometrical Product Specifications (GPS) - Surface texture: Profile method - Terms, definitions and surface texture parameters, Berlin, De, Standard, 2010, https://doi.org/10.31030/1699310.
[12] P.M. Santos, E.N. Júlio, A state-of-the-art review on roughness quantification methods for concrete surfaces, Constr. Build. Mater. 38 (2013) 912–923, https://doi.org/10.1016/j.conbuildmat.2012.09.045.
[13] ASTM E965– - 96, Standard Test Method for Measuring Pavement Macrotexture Depth Using a Volumetric Technique, Standard, West Conshohocken, PA, USA, 2001, p. 1996, https://doi.org/10.1520/E0965-96R01.
[14] S. China, D.E. James, Comparison of laser-based and sand patch measurements of pavement surface macrotexture, J. Transp. Eng. 138 (2) (2012) 176–181, https://doi.org/10.1061/(ASCE)TE.1943-5436.0000315.
[15] L. Yuan, J. Guo, Q. Wang, Automatic classification of common building materials from 3d terrestrial laser scan data, Autom. Constr. 110 (2020) 103017, https://doi.org/10.1016/j.autcon.2019.103017.
[16] K. Tan, X. Cheng, Correction of incidence angle and distance effects on tls intensity data based on reference targets, Remote Sens. 8 (3) (2016) 251, https://doi.org/10.3390/rs8030251.
[17] S. Kaasalainen, A. Jaakkola, M. Kaasalainen, A. Krooks, A. Kukko, Analysis of incidence angle and distance effects on terrestrial laser scanner intensity: search for correction methods, Remote Sens. 3 (10) (2011) 2207–2221, https://doi.org/10.3390/rs3102207.
[18] D. Bolkas, Terrestrial laser scanner intensity correction for the incidence angle effect on surfaces with different colours and sheens, Int. J. Remote Sens. 40 (18) (2019) 7169–7189, https://doi.org/10.1080/01431161.2019.1601283.
[19] M. Franceschi, G. Teza, N. Preto, A. Pesci, A. Galgaro, S. Girardi, Discrimination between marls and limestones using intensity data from terrestrial laser scanner, ISPRS J. Photogramm. Remote Sens. 64 (6) (2009) 522–528, https://doi.org/10.1016/j.autcon.2019.103017.
[20] C. Suchocki, J. Katzer, Terrestrial laser scanning harnessed for moisture detection in building materials–problems and limitations, Autom. Constr. 94 (2018) 127–134, https://doi.org/10.1016/j.autcon.2018.06.010.
[21] A. Valikhani, A. Jaberi Jahromi, S. Pouyanfar, I.M. Mantawy, A. Azizinamini, Machine Learning and Image Processing Approaches for Estimating Concrete Surface Roughness Using Basic Cameras, Computer-Aided Civil and Infrastructure Engineering, 2020, https://doi.org/10.1111/mice.12605.
[22] B. Özcan, R. Schwermann, J. Blankenbach, A novel camera-based measurement system for roughness determination of concrete surfaces, Materials 14 (1) (2021) 158, https://doi.org/10.3390/ma14010158.
[23] J. Bard, A. Bidgoli, W.W. Chi, Image classification for robotic plastering with convolutional neural network, in: Robotic Fabrication in Architecture, Art and Design, Springer, 2018, pp. 3–15, https://doi.org/10.1007/978-3-319-92294-2_1.
[24] S. Lee, H. Lim, S. Ahn, S. Lee, Ir surface reflectance estimation and material type recognition using two-stream net and kinect camera, in: ACM SIGGRAPH 2019 Posters, 2019, pp. 1–2, https://doi.org/10.1145/3306214.3338557.
[25] A. Pesci, G. Teza, et al., Effects of Surface Irregularities on Intensity Data from Laser Scanning: An Experimental Approach, Annals of Geophysics, 2008, https://doi.org/10.4401/ag-4462.
[26] M. Milenkovic, N. Pfeifer, P. Glira, Applying terrestrial laser scanning for soil surface roughness assessment, Remote Sens. 7 (2) (2015) 2007–2045, https://doi.org/10.3390/rs70202007.
[27] C.R. Harris, K.J. Millman, S.J. van der Walt, R. Gommers, P. Virtanen, D. Cournapeau, E. Wieser, J. Taylor, S. Berg, N.J. Smith, et al., Array programming with numpy, Nature 585 (7825) (2020) 357–362, https://doi.org/10.1038/s41586-020-2649-2.
[28] P. Virtanen, R. Gommers, T.E. Oliphant, M. Haberland, T. Reddy, D. Cournapeau, E. Burovski, P. Peterson, W. Weckesser, J. Bright, et al., Scipy 1.0: fundamental algorithms for scientific computing in python, Nat. Methods 17 (3) (2020) 261–272, https://doi.org/10.1038/s41592-019-0686-2.
[29] S. Van der Walt, J.L. Schönberger, J. Nunez-Iglesias, F. Boulogne, J.D. Warner, N. Yager, E. Gouillart, T. Yu, Scikit-image: image processing in python, PeerJ 2 (2014), e453, https://doi.org/10.7717/peerj.453.
[30] B. Langmann, K. Hartmann, O. Loffeld, Depth camera technology comparison and performance evaluation, in: ICPRAM (2), Citeseer, 2012, pp. 438–444, https://doi.org/10.5220/0003778304380444.
[31] R. Horaud, M. Hansard, G. Evangelidis, C. Ménier, An overview of depth cameras and range scanners based on time-of-flight technologies, Mach. Vis. Appl. 27 (7) (2016) 1005–1020, https://doi.org/10.1007/s00138-016-0784-4.
[32] M. Carfagni, R. Furferi, L. Governi, M. Servi, F. Uccheddu, Y. Volpe, On the performance of the intel sr300 depth camera: metrological and critical characterization, IEEE Sensors J. 17 (14) (2017) 4508–4519, https://doi.org/10.1109/JSEN.2017.2703829.
[33] Lucid Vision Labs, Helios Time of Flight (ToF) 3d Camera. URL. https://thinklucid.com/product/helios-time-of-flight-imx556/, 2020.
[34] G. Wolberg, Digital image warping, in: IEEE computer society press Los Alamitos, CA 10662, 1990. ISBN 978-0-818-68944-4.
[35] H. Hoppe, T. DeRose, T. Duchamp, J. McDonald, W. Stuetzle, Surface reconstruction from unorganized points, Computer Graphics (ACM) 26 (2) (1992) 71–78, https://doi.org/10.1145/133994.134011.
[36] E. Hecht, Optics 4th edition, Optics 1998 (1998) 1. ISBN 9780805385663.
[37] J.T. Barron, J. Malik, Shape, illumination, and reflectance from shading, IEEE Trans. Pattern Anal. Mach. Intell. 37 (8) (2014) 1670–1687, https://doi.org/10.1109/TPAMI.2014.2377712.
[38] N. Alldrin, T. Zickler, D. Kriegman, Photometric stereo with non-parametric and spatially-varying reflectance, in: 2008 *IEEE Conference on Computer Vision and Pattern Recognition*, IEEE, 2008, pp. 1–8, https://doi.org/10.1109/CVPR.2008.4587656.
[39] P.C. Joerg, J. Weyermann, F. Morsdorf, M. Zemp, M.E. Schaepman, Computation of a distributed glacier surface albedo proxy using airborne laser scanning intensity data and in-situ spectro-radiometric measurements, Remote Sens. Environ. 160 (2015) 31–42, https://doi.org/10.1016/j.rse.2014.12.017.
[40] B.T. Phong, Illumination for computer generated pictures, Commun. ACM 18 (6) (1975) 311–317, https://doi.org/10.1145/360825.360839.